# ANALYSIS OF VORTEX SHEDDING CHARACTERISTICS AND HEAT TRANSFER PERFORMANCE OF STAGGERED TUBE BUNDLE SYSTEM

***Yinlin JIAN [1], Bin DONG [1, 2], Shuyang FENG [1, 2], Dangguo YANG [1, 2], Yue LI [1, 2] ****

[*1] State Key Laboratory of Aerodynamics, Mianyang Sichuan 621000, China

[*2] High Speed Aerodynamics Institute, China Aerodynamics Research and Development Center, Mianyang Sichuan 621000, China

[*] Corresponding author; E-mail: liyue9663@163.com

*Tube bundle systems' heat transfer is unclear due to complex flow channels and turbulent fluctuations, affecting energy efficiency. This study simulates 2D staggered 18-row tube bundles at Reynolds numbers 3,100-50,000. 3D cylinders are simplified to 2D tubes, with grid independence and model validation. Flow, temperature fields, and synergy angles are analyzed for positions, Reynolds numbers, and spacings. High vortex shedding frequency in front tubes with multiple subfrequencies at different amplitudes. Asymmetric solutions emerge due to turbulent fluctuations. At high Reynolds, vortex shedding patterns complexify and frequencies rise. Nusselt number and synergy angle trends similar at low Reynolds, but diverge at high Reynolds. Small tube spacings significantly impact heat transfer; large spacings have weaker effects.*

Key words*: Vortex shedding frequency, Asymmetric flow, Gap flow, Tube bundle heat transfer, Synergy Angle.*

## 1. Introduction

In the energy field, heat exchange technology plays a pivotal role, which runs through the core processes of almost all modern industrial production. Shell-and-tube heat exchangers have become key equipment widely used in this field due to their excellent sealing and pressure resistance [1]. Among them, the flow around tube bundles and heat transfer characteristics are particularly crucial, which directly affect the performance and efficiency of the heat exchanger. In the study of flow around tube bundles, vortex shedding is a mechanical phenomenon that cannot be ignored. This phenomenon not only has a significant impact on the flow field structure, but also further affects the heat transfer characteristics of the tube bundles. Additionally, factors such as the position of the circular tubes, their compactness, and the Reynolds number (*Re*) of the fluid can all significantly influence vortex shedding. It is worth noting that due to the randomness and complexity of turbulent pulsations, asymmetric solutions may occur even at symmetric positions in the flow field [2]. This means that under the same conditions, circular tubes at different positions may exhibit different vortex shedding characteristics, leading to differences in local heat transfer. Therefore, a deep understanding of vortex shedding phenomena in circular tubes at different positions within tube bundle systems, the distribution of Nusselt numbers (*Nu*), and the influence of tube spacing is of great significance for enhancing the overall heat transfer capability of tube bundle systems.

In past research, many scholars have conducted studies on the enhancement of heat transfer between tube bundles. Some scholars have focused on optimizing the structure, studying different circular tube shapes and tube bundle arrangements [3]. For instance, in 2018, H. A. Refaey et al. [5] found that reducing the length-to-diameter ratio and selecting smaller-diameter flat tubes can improve heat transfer efficiency. In 2023, I. A. Popov et al. [8] enhanced turbulence by adding heat transfer augmentation elements (such as spherical dimples), thereby improving heat transfer performance. Other scholars, on the other hand, have focused on heat transfer mechanisms, analyzing flow and temperature fields under different operating conditions [10]. For example, in 2010, Y. Takemoto et al. [11] discovered through numerical simulations that within the range of $Re$ numbers where flow transitions from steady to oscillatory states, physical quantities such as the $Nu$ number and pressure loss may exhibit discontinuous jumps, attributed to hysteresis phenomena caused by multiple stable solutions in the flow. In 2011, J. H. Jeong et al. [12] compared the effects of two evaluation methods on convective heat transfer coefficients on the tube side and shell side, finding that the average nusselt number ($\overline{Nu}$) based on the LMTD method was 22.6% lower than that obtained using the surface temperature method.

Vortex generation, development, and shedding induce alternating pressure on cylinder surfaces, enhancing fluid-tube heat exchange and thus heat transfer. Recent studies on vortex shedding in circular tubes abound. In 2000, E. Konstantinidis et al. [14] utilized laser Doppler velocimetry and flow visualization to characterize flow around tandem tube bundles in steady and pulsating crossflows, observing a constant Strouhal number (St) of 0.14 in all rows except the first. In 2023, L. M. Qi [15] analyzed wake dynamics and cylinder interaction through time-averaged Reynolds stress near walls. In, 2023, L. C. Hsu et al. [16] explored five flow patterns' impacts on heat transfer. In 2024, P. Yin et al. [17] studied two-dimensional VIV of side-by-side cylinders near walls at low $Re$ (200), finding lock-in range, vibration, and wake patterns influenced by cylinder spacing and wall gap.

While many studies have explored flow and heat transfer in tube bundles, they mostly centered on vortex shedding, flow patterns in single or double tubes, and optimizations of tube shapes, arrangements, and compactness. However, research on tubes at varying positions within the bundle is scarce. This study fills that gap by numerically simulating an 18-row staggered tube bundle. By establishing reference positions, adjusting the $Re$ number, and modifying tube spacing, it delves into vortex shedding, flow, and heat transfer characteristics of tubes in different positions. Furthermore, it analyzes the temperature field distribution across the entire tube bundle system.

## 2. Numerical methods

### 2.1. Geometric model and boundary conditions

The geometric model of the staggered tube bundle system is shown in Fig. 1, and the flow is simplified into a two-dimensional flow problem for numerical simulation calculations. The transverse tube spacing is denoted as $S_1$, the longitudinal tube spacing is denoted as $S_2$, and the diameter of the circular tube is denoted as $D$. During the numerical calculations, to eliminate the influence of inlet and outlet effects, the inlet region length is set to 6 $D$, the outlet region length is set to 12 $D$, and the spacing between the upper and lower walls to the circular tube is set to 2.5 $D$. The simulation scheme is shown in Table 1.

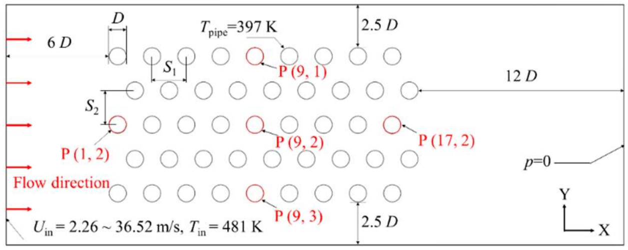


**Fig. 1 Geometric model diagram**

**Table 1. Numerical simulation scheme**

| Case | *Re* | $S_1$ | $S_2$ | Case | *Re* | $S_1$ | $S_2$ |
|---|---|---|---|---|---|---|---|
| 1 | 3100 | | | 7 | | 1.2 *D* | 2 *D* |
| 2 | 10,000 | | | 8 | | 2.6 *D* | 2 *D* |
| 3 | 20,000 | 2 *D* | 2 *D* | 9 | 3,100 | 4 *D* | 2 *D* |
| 4 | 30,000 | | | 10 | | 2 *D* | 1.2 *D* |
| 5 | 40,000 | | | 11 | | 2 *D* | 2.6 *D* |
| 6 | 50,000 | | | 12 | | 2 *D* | 4 *D* |

During the simulation, the inlet boundary condition is set as a velocity inlet, with a velocity range of $U_{in}$ = 2.26 to 36.52 m/s, corresponding to *Re* numbers of 3,100 to 50,000, and an inlet temperature of $T_{in}$ = 481 K. The outlet boundary condition is set as a pressure outlet with a gauge pressure $p$ = 0. The tube walls are assumed to be smooth and have a no-slip condition, with a tube wall temperature of $T_{pipe}$ = 397 K. To facilitate subsequent analysis, five circular tubes at specific positions are selected as analysis objects, namely P (1, 2), P (9, 1), P (9, 2), P (9, 3), and P (17, 2).

## 2.2. Mathematical model and characterization parameters

To simplify the problem of staggered tube bundle flow and heat transfer, the following assumptions are made: (a) The physical properties of the fluid are considered constant, and it is treated as an incompressible Newtonian fluid; (b) The effects of thermal radiation, gravity, and buoyancy are neglected. Since it is necessary to solve the instantaneous value of the lift coefficient for the purpose of analyzing the lift coefficient spectrum, an unsteady solution method is adopted. The simplified two-dimensional unsteady governing equations obtained are as follows,

Continuity equation,

$$\frac{\partial \rho}{\partial t}+\frac{\partial\left(\rho U_i\right)}{\partial x_i}=0 \tag{1}$$

Momentum equation,

$$\frac{\partial\left(\rho U_i\right)}{\partial t}+\frac{\partial\left(\rho U_j U_i\right)}{\partial x_j}=-\frac{\partial p}{\partial x_i}+\mu \nabla^2 u_i \tag{2}$$

Energy equation,

$$c_p\left[\frac{\partial(\rho T)}{\partial t}+\frac{\partial\left(\rho U_j T\right)}{\partial x_j}\right]=\frac{\partial}{\partial x_j}\left(\lambda_f \frac{\partial T}{\partial x_j}\right) \tag{3}$$

where $\rho$ represents the fluid density, kg/m³; $u$ is the fluid velocity, m/s; $x$ is the spatial coordinate, m; $t$ is the time, s; $i$ and $j$ are dummy indices; $p$ is the pressure, Pa; $\mu$ is the fluid viscosity, Pa·s; $\nabla^2$ is the

Laplacian operator; $c_p$ is the specific heat capacity, J/(kg·K); $T$ is the thermodynamic temperature, K; and $\lambda_f$ is the fluid thermal conductivity, W/(m·K).

The turbulence model adopts the standard $k$-$\varepsilon$ bipartite model,

$$\frac{\partial \rho k}{\partial t}+\frac{\partial \rho k U_i}{\partial x_i}=\frac{\partial}{\partial x_j}\left[\left(\mu+\frac{\mu_t}{\sigma_k}\right)\frac{\partial k}{\partial x_j}\right]+G_k-\rho\varepsilon \tag{4}$$

$$\frac{\partial\left(\rho\varepsilon U_i\right)}{\partial t}=\frac{\partial}{\partial x_j}\left[\left(\mu+\frac{\mu_t}{\sigma_\varepsilon}\right)\frac{\partial \varepsilon}{\partial x_j}\right]+\frac{\varepsilon}{k}\left(C_{1\varepsilon}G_k-C_{2\varepsilon}\varepsilon\rho\right) \tag{5}$$

where $k$ represents the turbulent kinetic energy, m²/s²; $\varepsilon$ represents the turbulent dissipation rate, m²/s³; $G_k$ is the generation term of turbulent kinetic energy; $\mu_t$ is the turbulent viscosity, Pa·s, and its calculation formula is,

$$\mu_t=\rho C_\mu\frac{k^2}{\varepsilon} \tag{6}$$

In the turbulence model, $C_{1\varepsilon}$, $C_{2\varepsilon}$, $C_\mu$, $\sigma_k$, and $\sigma_\varepsilon$ are constants, with values of 1.44, 1.92, 0.09, 1.0, and 1.3, respectively [19]. The SIMPLE algorithm is used to solve the Navier-Stokes equations. QUICK scheme is adopted for the discretization of the convection term, second-order implicit discretization scheme is used for the transient term, and the solution time step is set to 0.001 s.

Before analyzing the lift coefficient spectrum, it is necessary to define the lift coefficient $C_L$, and its definition is as follows,

$$C_L=\frac{F_L}{0.5\rho U_\infty^2 LD} \tag{7}$$

where $F_L$ represents the surface lift force acting on a two-dimensional cylinder, in Newtons (N); $U_\infty$ is the free stream velocity, m/s; $L$ is the length of the tube, which in a two-dimensional problem is taken as 1; and $D$ is the diameter of the tube.

When analyzing heat transfer problems, it is necessary to define the local convective heat transfer coefficient $h_{local}$, local Nusselt number $Nu_{local}$, and average Nusselt number $\overline{Nu}$ separately,

$$h_{local}=-\lambda_f\frac{\partial T}{\partial n}D \tag{8}$$

$$Nu_{local}=\frac{h_{local}D}{\lambda_f} \tag{9}$$

$$\overline{Nu}=\frac{1}{2\pi}\int_0^{2\pi}Nu_{local}\mathrm{d}\theta \tag{10}$$

where $n$ represents the normal vector of the pipe wall, and $\theta$ is the angle, rad.

### 2.3. Grid model and independence verification

As depicted in Fig. 2, Unstructured grids are used for the whole flow field, and the grid around the circular pipe is refined. Subsequently, seven sets of grids with varying node counts were utilized to conduct a grid independence verification on the $\overline{Nu}$ of the circular tube. The verification results are shown in Fig. 3.

$\overline{Nu}$ of the circular tube. The verification results are shown in Fig. 3.

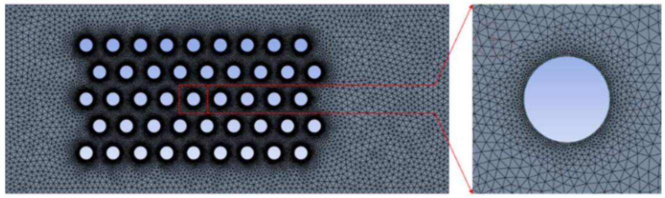

**Fig. 2 Grid and local magnification**

As shown in Fig. 3, when the number of grid nodes exceeds 42,011, the deviation in the $\overline{Nu}$ is already less than 1%. In order to balance the computational accuracy and cost, a grid with 42,011 nodes is selected for numerical calculation. It should be noted that when the geometric structure changes, the number of grid nodes needs to be adjusted accordingly, but the overall and local growth rates of grid size as well as the grid division method should remain unchanged.

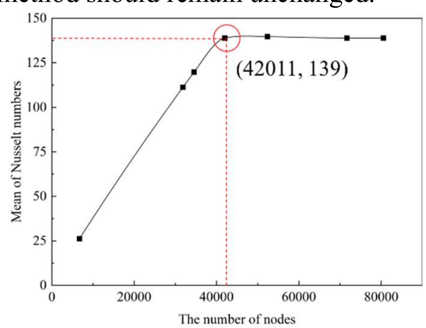


**Fig. 3 Grid independence verification results**

## 2.4. Validation of numerical model

To ensure the correctness of the mathematical model, Case 1 was selected for numerical simulation. The numerical results of the $\overline{Nu}$ for the circular tube were compared with the Zukauskas correlation, and the results showed that the average deviation was 8.01% with a minimum deviation of 4.91%. This indicates that the mathematical model adopted is correct and can proceed with subsequent numerical simulation studies.

When $Re$ falls within the range of [1,000, 200,000], and the number of tube rows is greater than or equal to 16, the Zukauskas correlation is defined as follows,

$$Nu = 0.27 Re^{0.63} Pr_{\mathrm{f}}^{0.36} \left( Pr_{\mathrm{f}} / Pr_{\mathrm{w}} \right)^{0.25} \tag{11}$$

where $Pr_f$ is determined based on the average temperature of the inlet and outlet cross-sections, while $Pr_w$ is determined based on the wall temperature of the pipe. Both of these are dimensionless parameters [18].

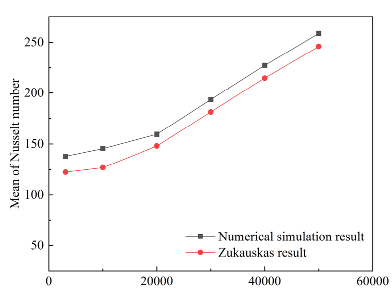


**Fig. 4 Model verification results**

## 3. Results and discussion

### 3.1. Analysis of vortex shedding frequency

#### *3.1.1 Vortex shedding frequency of circular tubes at different positions in the flow direction*

In order to analyze the vortex shedding frequency of the circular tubes, the Fast Fourier Transform (FFT) is used to convert the time-domain characteristics of the lift coefficient on the surface of the circular tubes into frequency-domain characteristics. P (1, 2), P(9, 2), and P (17, 2) are selected as the analysis objects because these three circular tubes are located at the front, middle, and rear positions in the flow direction, respectively, and are representative.

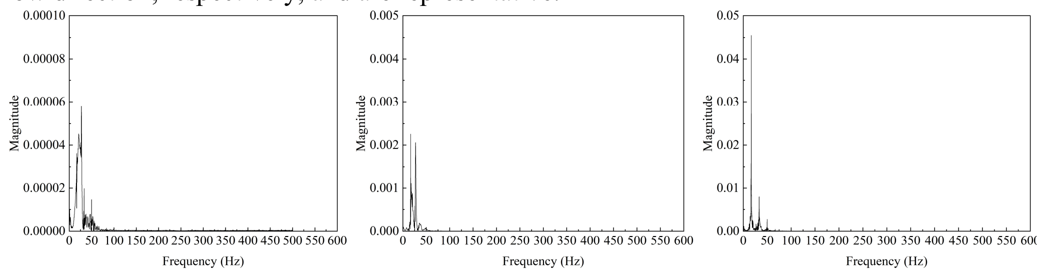


(a) (b) (c)

**Fig. 5 Spectral diagram of lift coefficient of circular tubes at different positions in the flow direction. (a) P (1, 2), (b) P (9, 2), (c) P (17, 2)**

As shown in Fig. 5, by observing the frequency corresponding to the maximum amplitude in the graph, the vortex shedding frequencies of P (1, 2), P (9, 2), and P (17, 2) are 27.2 Hz, 16.6 Hz, and 16.6 Hz respectively. This indicates that the closer the circular tube is to the upstream, the higher the vortex shedding frequency, due to its greater incoming flow velocity (Fig. 6). Although P (9, 2) and P (17, 2) have the same vortex shedding frequency, the amplitude of P (17, 2) is approximately 20 times that of P (9, 2), indicating that their vortex shedding patterns are similar, but the vortex shedding contribution of P (17, 2) is greater. In fact, as shown in Fig. 7, the vortex distribution near P (17, 2) confirms this, as it is evident that the upper vortex of P (17, 2) has a greater intensity.

Moreover, from the lift coefficient spectrum graphs of circular tubes at different positions, it can be observed that there are multiple frequencies. The reasons are as follows: As seen in Fig. 6, for P (1, 2), it is influenced by the undisturbed gap flow; for P (9, 2), although the impact of the gap flow is minimal, it is affected by the wake vortices from upstream tubes, resulting in a vortex shedding pattern that is a superposition of upstream and its own; for P (17, 2), the significantly deflected gap flow significantly affects the vortex shedding process, while it is also influenced by upstream effects.

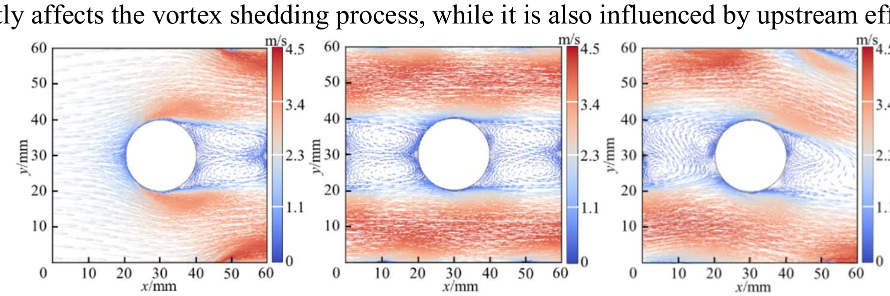


(a) (b) (c)

**Fig. 6 Velocity vector distribution near the circular tube at different positions along the flow direction. (a) P (1, 2), (b) P (9, 2), (c) P (17, 2)**

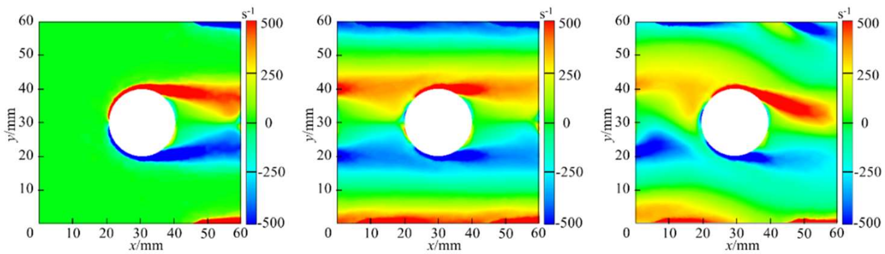


(a) (b) (c)

**Fig. 7 Vorticity distribution around circular tubes at different positions along the flow direction. (a) P (1, 2), (b) P (9, 2), (c) P (17, 2)**

### *3.1.2 Asymmetric characteristics of vortex shedding frequency of circular tube in symmetrical position*

Due to the nonlinearity of the flow control equation and the presence of a certain amount of pulsation and turbulence in the flow field, the vortex shedding frequency of circular tubes exhibits asymmetric phenomena [20]. Specifically, even if the entire tube bundle model is geometrically symmetric, the vortex shedding frequencies of mutually symmetric circular tubes are different. Circular tubes P (9, 1) and P (9, 3) are located in symmetrical positions on the ninth row. From the lift coefficient spectrum chart, their vortex shedding frequencies are 18.3 Hz and 16.6 Hz, respectively, with corresponding lift coefficient amplitudes of 0.0027 and 0.0042 (Fig. 8). This, to a certain extent, reflects the asymmetric nature of the vortex shedding frequency distribution.

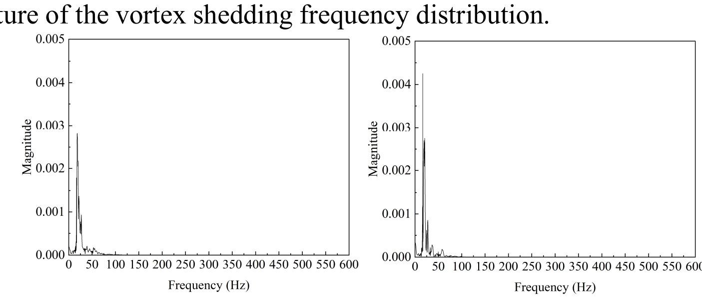


(a) (b)

**Fig. 8 Spectral diagram of lift coefficient of circular tube in symmetrical position. (a) P (9, 1), (b) P (9, 3)**

In order to further explore the direct cause of the asymmetric distribution of vortex shedding frequency, the vorticity distribution around the circular tube is extracted. As shown in Fig. 9, from the vorticity distribution diagrams of P (9, 1) and P (9, 3), it can be observed that the average vorticity around P (9, 1) is greater, indicating that the vortex strength on the windward and leeward sides of P (9, 1) is stronger. This is the direct reason why the vortex shedding frequency of P (9, 1) is slightly higher than that of P (9, 3).

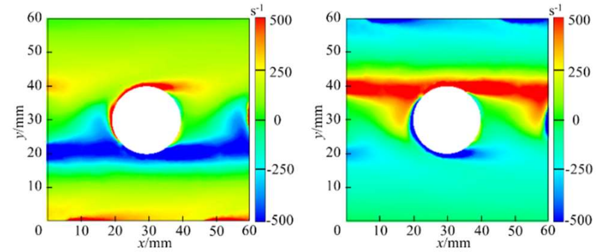


(a) (b)

**Fig. 9 Vorticity distribution near the circular tube in symmetrical position. (a) P (9, 1), (b) P (9, 3)**

### *3.1.3 Influence of Re number on vortex shedding frequency*

To investigate the effect of *Re* number on vortex shedding frequency, Cases 1 to 6 were simulated, and circular tube P (9, 2) was selected as a reference to analyze its lift coefficient spectrum. As shown in Fig. 10, as the *Re* number gradually increases, the vortex shedding frequency also increases. However, when the *Re* number reaches or exceeds 40,000, the vortex shedding frequency remains almost unchanged, indicating that the *Re* number has little impact on vortex shedding frequency under these conditions.

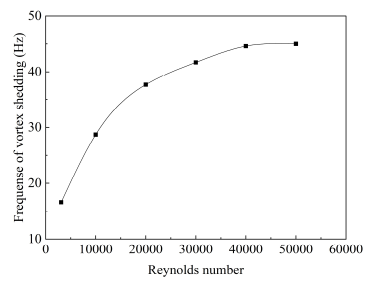


**Fig. 10 Influence of *Re* number on P (9, 2) vortex shedding frequency**

As shown in Figure 11, when *Re* = 3,100, the vortex shedding frequency is 16.6 Hz accompanied by a secondary frequency of 27.1 Hz. However, when *Re* = 50,000, the vortex shedding frequency is 43.5 Hz and accompanied by four other more prominent secondary frequencies, which are 14.5 Hz, 72.4 Hz, 138.8 Hz, and 231.6 Hz. This indicates that at high *Re* numbers, the vortex shedding pattern of the circular tube is formed by the superposition of multiple periods. Conversely, at lower *Re* numbers, the vortex shedding pattern of the circular tube is more singular.

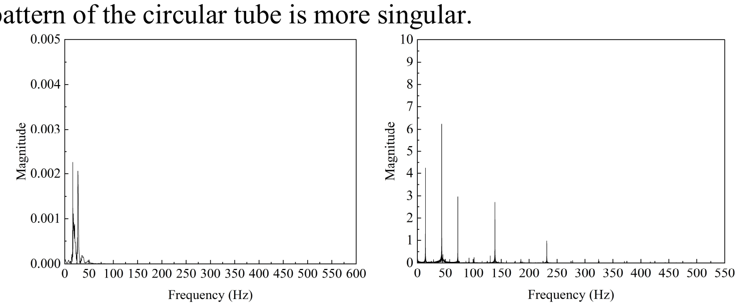


(a) (b)

**Fig. 11 Spectral diagram of lift coefficient of P (9, 2) at low and high *Re* numbers; (a) *Re* = 3,100, (b) *Re* = 50,000**

As shown in Fig. 12, observing the velocity vector distribution near the circular tube under low and high Re numbers, when $Re$ = 3,100, the vortices on the windward and leeward sides of the circular tube are symmetrically distributed up and down, with no significant influence from the gap flow. However, when $Re$ = 50,000, the vortex distribution on the windward and leeward sides of the circular tube is significantly affected by the skewed gap flow. This once again confirms the impact of $Re$ number on vortex shedding from the circular tube, namely, that under high $Re$ number flow, the vortex shedding pattern of the circular tube is more complex, resulting in a higher vortex shedding frequency.

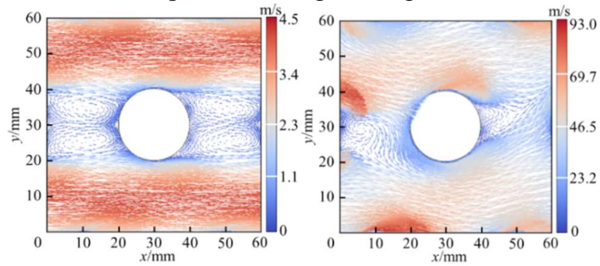


(a) (b)

**Fig. 12 Velocity vector distribution near P (9, 2) under low and high *Re* numbers; (a) *Re* = 3,100, (b) *Re* = 50,000**

## 3.2. Flow field and heat transfer analysis

### *3.2.1 Effect of tube spacing*

To investigate the effect of tube spacing on heat transfer, Cases 7 to 12 were simulated. As shown in Fig. 13, with the increase in the transverse pipe spacing ($S_1$), the $\overline{Nu}$ number first increases, but the increase becomes slower and slower. Meanwhile, as the longitudinal pipe spacing ($S_2$) increases, the $\overline{Nu}$ number first decreases, and the decrease also becomes slower and slower. When the transverse pipe spacing ($S_1$) increases from 1.2 $D$ to 4 $D$, the increase in the $\overline{Nu}$ number is 1.8% and 0%, respectively. When the longitudinal pipe spacing ($S_2$) increases from 1.2 $D$ to 4 $D$, the decrease in the $\overline{Nu}$ number is -3.4% and -0.6%, respectively. This indicates that when the pipe spacing is small, changes in the longitudinal pipe spacing are more likely to alter the heat transfer performance. However, when the pipe spacing is large, the impact of pipe spacing on heat transfer performance is relatively small.

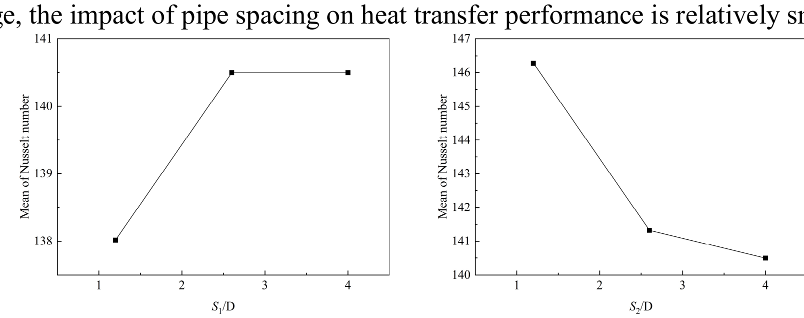


(a) (b)

**Fig. 13 Influence of tube spacing on the $\overline{Nu}$ number. (a) different $S_1$, (b) different $S_2$**

As shown in Fig. 14, based on the temperature contour map, the larger the transverse tube spacing $S_1$ is, the more uniform the temperature distribution becomes. Conversely, the larger the longitudinal tube spacing $S_2$ is, the less uniform the temperature distribution is. When the longitudinal tube spacing

$S_2$ is relatively large, the deflection of the gap flow is significant. Combined with the analysis of vortex shedding around circular tubes mentioned in the previous text, this will significantly affect the flow conditions within the tube bundle, thereby influencing heat exchange performance.

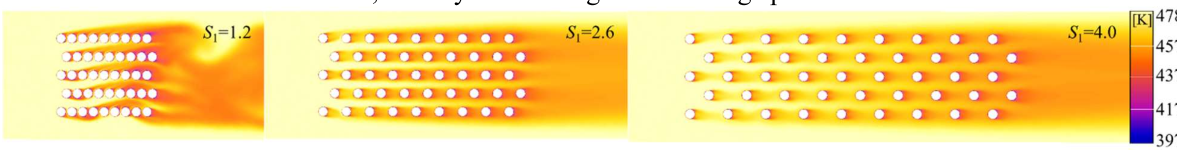


(a)

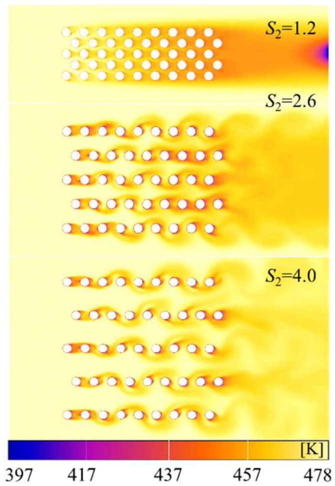


(b)

**Fig. 14 Temperature field under different tube spacing. (a) different $S_1$, (b) different $S_2$**

To conduct a more detailed analysis of the $Nu_{local}$ on the surface of the circular tube, the distribution of $Nu_{local}$ on the surface of circular tube P (9, 2) was extracted. As shown in Fig. 15(a), when the transverse tube spacing $S_1$ is 1.2 *D*, 2.6 *D*, and 4 *D*, the maximum values of the $Nu_{local}$ number are located at 18°, 144°, and 324°, respectively, while the minimum values are located at 342°, 252°, and 198°, respectively. As shown in Fig. 16(b), when the longitudinal tube spacing $S_2$ is 1.2 *D*, 2.6 *D*, and 4 *D*, the maximum values of the $Nu_{local}$ number are located at 54°, 234°, and 234°, respectively, while the minimum values are located at 126°, 0°, and 342°, respectively.

When the horizontal tube spacing is at its minimum, the location with the highest $Nu_{local}$ number is at 18°, while the location with the lowest $Nu_{local}$ number is at 342°, and these two locations are exactly symmetric about the horizontal central axis of the circular tube. When the horizontal tube spacing is at its maximum, the location with the highest $Nu_{local}$ number is at 324°, while the location with the lowest $Nu_{local}$ number is at 198°. When the vertical tube spacing is at its minimum, the location with the highest $Nu_{local}$ number is at 54°, while the location with the lowest $Nu_{local}$ number is at 126°, and these two locations are exactly symmetric about the vertical central axis of the circular tube. When the vertical tube spacing is at its maximum, the location with the highest $Nu_{local}$ number is at 234°, while the location with the lowest $Nu_{local}$ number is at 342°.

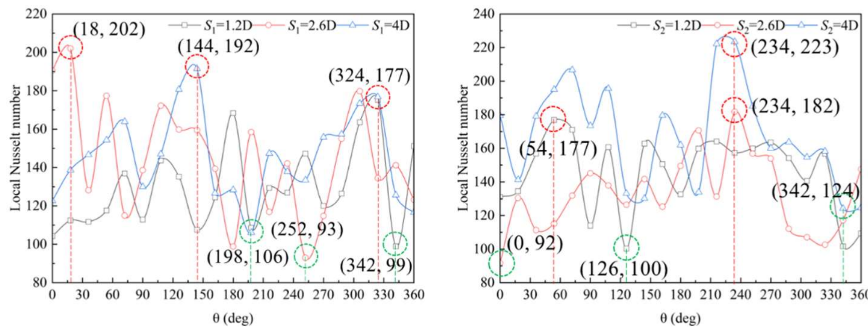


(a) (b)

**Fig. 15 $Nu_{local}$ number distribution of P (9, 2) at different tube spacing. (a) different $S_1$, (b) different $S_2$**

According to the field synergy principle, the smaller the angle between the velocity field and the temperature gradient field, the higher the heat transfer intensity. This is because a smaller angle indicates a better degree of synergy between the velocity field and the temperature gradient field, resulting in more efficient heat exchange between the fluid and the wall. The synergy angle $\beta$ is defined as follows:

$$\beta = \arccos\left|\frac{\vec{U}\cdot\Delta\vec{T}}{\left|\vec{U}\right|\cdot\left|\Delta\vec{T}\right|}\right| \tag{12}$$

To measure the intensity of heat transfer near the circular tube, the synergy angle distribution around circular tube P (9, 2) was analyzed. As shown in Fig. 16, when the lateral tube spacing is small (Fig. 16(a)), the positions with the smallest synergy angle distribution are located below the stagnation point and in the shear layer, rather than at the stagnation point itself. This is because the gap flow significantly affects the synergy between the velocity and temperature gradient directions. When the transverse tube spacing increases (Fig. 16(b) and (c)), it can be found that the synergy angle is the smallest near the leading stagnation point and in the wake region of the shear layer. This is because, as the lateral spacing increases, the influence of upstream trailing vortices and gap flow on the circular tube weakens. The larger the lateral spacing, the smaller the upstream influence. When the lateral spacing is the largest, only the synergy angle at the windward face stagnation point is the smallest (Fig. 16(c)), indicating that the circular tube is hardly affected by upstream trailing vortices at this point. It also suggests that excessively large lateral tube spacing can also reduce the heat transfer intensity.

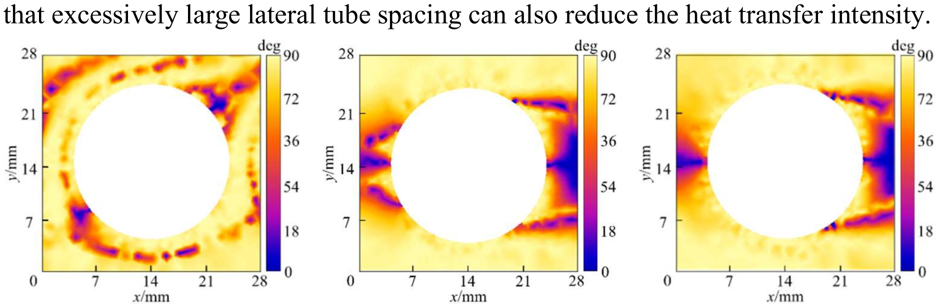


(a) (b) (c)

**Fig. 16 Distribution of synergy angle near P (9, 2) under different $S_1$ conditions. (a) $S_1$=1.2 $D$, (b) $S_1$=2.6 $D$, (c) $S_1$=4 $D$**

The variation in the longitudinal spacing of tubes in heat transfer certainly enhances or weakens the effect of the gap flow, thereby significantly affecting the uneven distribution of the temperature field.

As seen in Fig. 17, the distribution of the synergy angle is also similarly affected. When the longitudinal tube spacing is at its minimum (Fig. 17(a)), the positions with the smallest synergy angle are near the stagnation point and in the wake shear layer, resembling the situation when the lateral tube spacing is large. As the longitudinal tube spacing increases, the deflection of the gap flow becomes more severe, resulting in a highly asymmetrical distribution of the synergy angle. Additionally, the synergy angle at the stagnation point and in the wake shear layer increases (Fig. 17(b), (c)), indicating that increasing the longitudinal tube spacing will significantly reduce the heat transfer intensity.

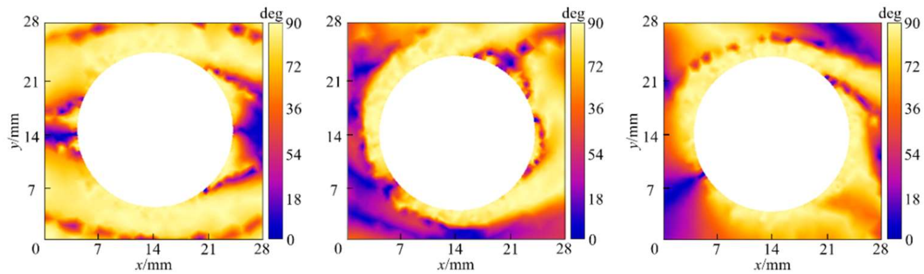


(a) (b) (c)

**Fig. 17 Distribution of synergy angle near P (9, 2) under different $S_2$ conditions. (a) $S_2$=1.2 $D$, (b) $S_2$=2.6 $D$, (c) $S_2$=4 $D$**

### *3.2.2 Heat transfer characteristics of circular tubes at different positions in the flow direction*

When fluid flows through a tube bundle heat exchanger system, the heat transfer efficiency of circular tubes at different locations varies, similar to the "wooden bucket principle," where the focus is on improving the areas with poor heat transfer performance. Therefore, it is crucial to study the heat transfer performance of circular tubes at different locations. Therefore, three circular tubes at different locations in the flow direction are selected as the research objects, which are P (1, 2), P (9, 2), and P (17, 2), respectively.

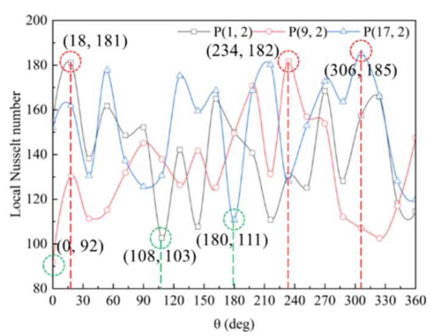


**Fig. 18 $Nu_{local}$ number distribution of circular tubes at different positions in the flow direction**

As shown in Fig. 18, the minimum value of the $Nu_{local}$ number for P (1, 2) is located at 108°, the minimum value for P (9, 2) is located at 0°, and the minimum value for P (17, 2) is located at 180°. To more intuitively observe the changing trend of the minimum $Nu_{local}$ position with the location of the circular tubes, the minimum $Nu_{local}$ positions of the circular tubes at three different locations are uniformly marked in Fig. 19. From Fig. 19, it can be seen that the minimum $Nu_{local}$ number for P (1, 2) is located in the shear layer, the minimum for P (9, 2) is located at the stagnation point, and the minimum for P (17, 2) is located at the center of the tail. This indicates that as the circular tube moves further back, the position of the minimum $Nu_{local}$ number gradually rotates counterclockwise from the upper shear layer, which is conducive to precisely improving the convection conditions near the circular tubes at different locations.

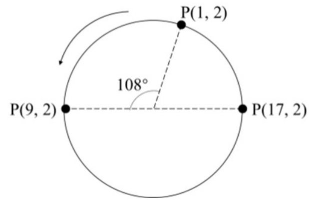


**Fig. 19 Minimum distribution of $Nu_{local}$ number of round tubes at different positions**

To further analyze the heat transfer intensity of circular tubes at different locations in the flow direction, the contour plots of the synergy angle distribution near P (1, 2) and P (17, 2) were extracted respectively. As shown in Fig. 20, the minimum synergy angles for the circular tube P (1, 2) are symmetrically distributed at the stagnation point, shear layer, and the center of the tail (Fig. 20(a)), which is because P (1, 2) is not significantly affected by the interstitial flow. However, the distribution of the synergy angle around the circular tubes P (9, 2) and P (17, 2) is not symmetrical (Fig. 20(b) and (c)), indicating that the circular tubes located further back in the tube bundle system are more strongly affected by the interstitial flow.

Moreover, there is a commonality in the distribution of the synergy angle near the circular tubes at the three locations, which is that the synergy angle in the wake vortex region is generally larger, indicating poor heat transfer performance in this area. From the perspective of improving heat transfer, the focus is on reducing the effect of interstitial flow in the tube bundle system and improving the vortex distribution in the wake region of the circular tubes, such as reducing the vortex scale and its influence range.

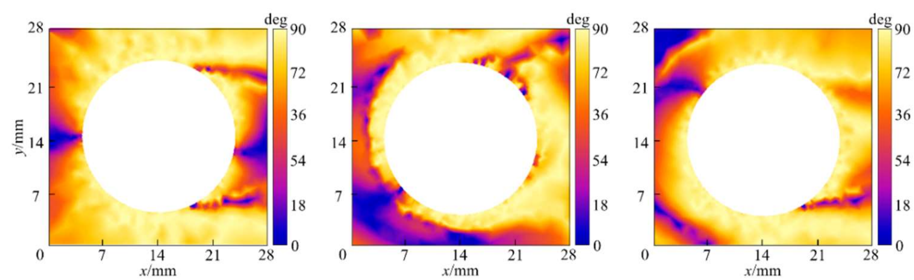


(a) (b) (c)

**Fig. 20 Distribution of synergy angles of circular tubes at different positions in the flow direction. (a) P (1, 2), (b) P (9, 2), (c) P (17, 2)**

### *3.2.3 The effect of Re number*

This subsection selects the simulation results of Cases 1 to 6 for analysis. From a theoretical perspective, the greater the Re number, the higher the turbulence level, and the more active the convective heat transfer. However, as analyzed previously, in certain vortex distribution regions, increasing the *Re* number can actually reduce the synergy angle in that region, which is not conducive to heat transfer. To investigate the changes in heat transfer effectiveness caused by variations in *Re* number, taking circular tube P (9, 2) as an example, the effects of *Re* number on $Nu_{local}$ and synergy angle distribution were analyzed. As shown in Fig. 21, the $Nu_{local}$ number distribution curves under different *Re* numbers all exhibit a characteristic of being high on both sides and low in the middle, and the curves in the middle region change relatively little compared to the sides. This indicates that changes in *Re* number are not likely to significantly improve convective heat transfer in the wake region.

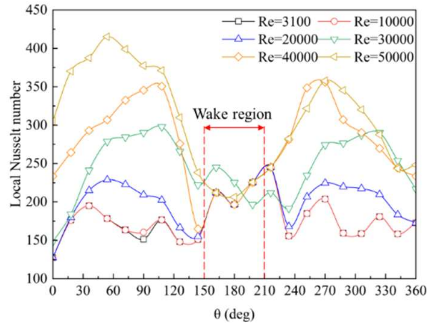


**Fig. 21 $Nu_{local}$ number distribution of P (9, 2) under different *Re* numbers**

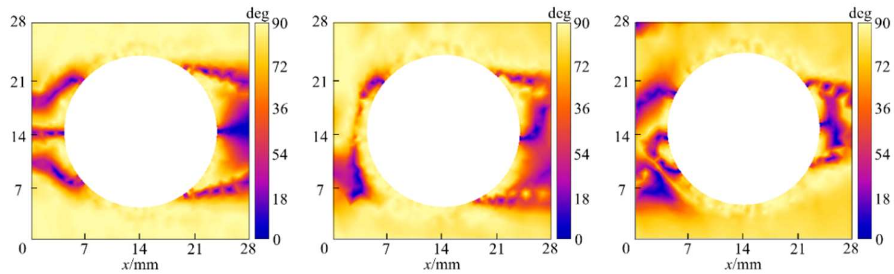


(a) (b) (c)

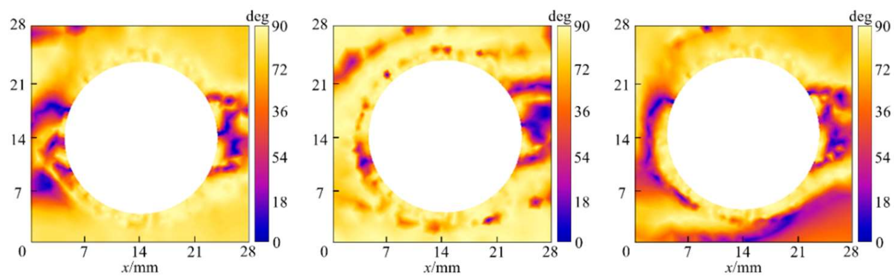


(d) (e) (f)

**Fig. 22 Distribution of synergy angles around P (9, 2) under different *Re* numbers. (a) *Re* = 3,100, (b) *Re* = 10,000, (c) *Re* = 20,000, (d) *Re* = 30,000, (e) *Re* = 40,000, (f) *Re* = 50,000**

To visually observe the change in the position of the minimum $Nu_{local}$ on the surface of the circular tube with *Re* number, the positions of the minimum $Nu_{local}$ under different *Re* numbers are uniformly marked in Fig. 23. As shown in Fig. 23, when *Re* number is between 3,100 and 30,000, the $Nu_{local}$ number is located at the stagnation point in the front. When *Re* = 40,000, the minimum $Nu_{local}$ value shifts to the edge of the wake region. And when *Re* = 50,000, the minimum $Nu_{local}$ value is positioned at the center of the tail. This indicates that as the *Re* number gradually increases, the position of the minimum $Nu_{local}$ value rotates clockwise from the stagnation point.

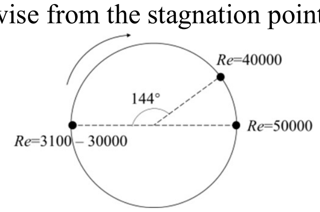


**Fig. 23 Minimum distribution of $Nu_{local}$ numbers under different *Re* numbers**

## 4. Conclusions

This paper simulates the unsteady flow in a two-dimensional staggered tube bundle system with 18 rows. By varying the *Re* number, tube spacing, and setting the reference position, the distribution of vortex shedding frequency, flow field, temperature field, and field synergy angle are analyzed. The following conclusions are drawn,

(1) The vortex shedding frequency of the front tubes in the flow direction is high, with less influence from the surroundings, but there are multiple frequencies with different amplitudes. To improve heat exchange, the impact of clearance flow and the vortex distribution in the wake region needs to be reduced.

(2) Due to the randomness and complexity of turbulent pulsations, the vortex shedding frequencies of tubes at symmetrical positions are different, this indicates that asymmetric flow patterns have emerged in the flow field.

(3) At high *Re* numbers, there are more secondary frequencies, resulting in a more complex vortex shedding pattern with higher frequencies. When the *Re* numbers are 3,100 and 50,000 respectively, the vortex shedding frequencies are 16.6 Hz and 43.5 Hz, respectively. The *Nu* number and the synergy angle exhibit similar trends under low *Re* number flows, but significant differences are observed under high *Re* number flows.

(4) In terms of the geometric layout of the tube bundle, when the tube spacing is small, changes in the longitudinal spacing have a significant impact on heat exchange performance. Conversely, when the tube spacing is large, regardless of changes in the horizontal or vertical spacing, the impact on heat exchange performance is relatively weak. When the transverse tube spacing $S_1$ increases from 1.2 $D$ to 4 $D$, the increase in the average *Nu* number is 1.8% and 0% respectively. When the longitudinal tube spacing $S_2$ increases from 1.2 $D$ to 4 $D$, the decrease in the average *Nu* number is -3.4% and -0.6% respectively.


## Acknowledgement

This research was funded by the National Natural Science Foundation of China (12272399, 52130603) and the Key Project of Sichuan Provincial Natural Science Foundation (2023NSFSC0006). We are extremely grateful to Bin Dong, Shuyang Feng, Dangguo Yang and Yue Li for their contributions to data processing and theoretical aspects.


## Nomenclature

$c_p$ – Specific heat capacity, [J·kg$^{-1}$·K$^{-1}$)]

$C_L$ – Lift coefficient (=2$F_L$·$\rho^{-1}$·$U_\infty^{-2}$·$L^{-1}$·$D^{-1}$), [-]

$D$ – Diameter of the circular tube, [m]

$F_L$ – Surface lift force, [N]

$G_k$ – Generation term of turbulent kinetic energy

$h_{local}$ – Local convective heat transfer coefficient, [W·m$^{-2}$·K$^{-1}$]

$k$ – Turbulent kinetic energy, [m$^2$·s$^{-2}$]

$L$ – Length of the tube, [m]

$n$ – Normal vector of the pipe wall

$Nu$ – Nusselt number, [-]

$\overline{Nu}$ – Average nusselt number, [-]

$Nu_{local}$ – Local nusselt number, [-]

$p$ – Pressure, [Pa]

$Pr_f$ – Fluid prandtl number, [-]

$Pr_w$ – Near wall prandtl number, [-]

$Re$ – Reynolds number (=$\rho$·$U_{\text{in}}$·$D$·$\mu^{-1}$), [-]

$S_1$ – Transverse tube spacing (=$x$·$D^{-1}$), [-]

$S_2$ – Longitudinal tube spacing ($=x\cdot D^{-1}$), [-]

$t$ – Time, [s]

$T$ – Temperature, [K]

$T_{in}$ – Inlet temperature, [K]

$T_{pipe}$ – Pipe wall temperature, [K]

$U_i$, $U_j$ – Velocity, [$m\cdot s^{-1}$]

$U_\infty$ – Free stream velocity, [$m\cdot s^{-1}$]

$U_\infty$ – Free stream velocity, [$m\cdot s^{-1}$]

$U_{\text{in}}$ – Inlet velocity, [$m\cdot s^{-1}$]

$x$ – Spatial coordinate, [m]

**Greek symbols**

$\rho$ – Fluid density, [$kg\cdot m^{-3}$]

$\mu$ – Fluid viscosity, [$Pa\cdot s$]

$\mu_t$ – Turbulent viscosity, [$Pa\cdot s$]

$\nabla^2$ – Laplacian operator

$\lambda_f$ – Fluid thermal conductivity, [$W\cdot m^{-1}\cdot K^{-1}$]

$\varepsilon$ – Turbulent dissipation rate, [$m^3\cdot s^{-3}$]

$\beta$ – Synergy angle, [deg]

$\theta$ – Coordinates of points on the surface of the tube, [rad]

**Subscripts**

pipe – Cylindrical tube surface

in – Inlet

1 – Landscape orientation

2 – Longitudinal

$i$, $j$ – Dummy index

$f$ – Fluid

$\infty$ – Free stream

*local* – The local position of the surface of the round tub

**References**


[1] Jiao F, et al., Effects of Tube Arrangements and Longitudinal Tube Spacing on Heat Transfer Performance of Heat Exchanger, Acta Petrolei Sinica (Petroleum Processing Section), 29 (2013), pp. 836-843.

[2] Wang H, et al., Mechanism Analysis of Asymmetric Flow in the Boiler Furnace with a Symmetrical Structure, Journal of Engineering Thermophysics, 34 (2013), pp. 2162-2165.

[3] Horvat A, et al., Comparison of heat transfer conditions in tube bundle cross-flow for different tube shapes, International Journal of Heat and Mass Transfer, 49 (2006), pp. 1027-1038.

[4] Wang Y. H, et al., Numerical Simulation of the Convection-based Heat Exchange Characteristics Outside Spirally Grooved Tube Bundles, Journal Of Engineering For Thermal Energy And Power, 29 (2014), pp. 509-514.

[5] Refaey H A, et al., Numerical investigations of the convective heat transfer from turbulent flow over staggered tube bank, Journal of The Institution of Engineers, 100 (2019), pp. 983-993.

[6] Yuan Y, et al., Analysis of influence of tube spacing on heat transfer of transverse tube bundle and nonlinear phenomenon, Energy saving and environmental protection, 6 (2020), pp. 57-67.

[7] Deeb R, Numerical analysis of the effect of longitudinal and transverse pitch ratio on the flow and heat transfer of staggered drop-shaped tubes bundle, International Journal of Heat and Mass Transfer, 183 (2022), pp. 122123.

[8] Popov I A, et al., Heat Transfer and Hydraulic Losses of Tube Bundles with Vortex Generators Indented on their Surface, Journal of Engineering Physics and Thermophysics, 96 (2023), pp. 1576-1592.

[9] Hishikar P, et al., Heat transfer analysis of nine cylinders arranged inline and staggered at subcritical Reynolds number, Numerical Heat Transfer, Part A: Applications (2024), pp. 1-22.

[10] Wu Z, et al., Experimental investigation on heat transfer characteristics of staggered tube bundle heat exchanger immersed in oscillating flow, International Journal of Heat and Mass Transfer, 148 (2020), pp. 119125.

[11] Takemoto Y, et al., Heat transfer in the flow through a bundle of tubes and transitions of the flow, International journal of heat and mass transfer, 2010, 53(23-24), pp. 5411-5419.

[12] Jeong J H, et al., The effects of the evaluation method on the average heat transfer coefficient for a mini-channel tube bundle, International journal of heat and mass transfer, 54 (2011), pp. 5481-5490.

[13] Mikheev N I, et al., Hydrodynamics and heat transfer of pulsating flow around a cylinder, International Journal of Heat and Mass Transfer, 109 (2017), pp. 254-265.

[14] Konstantinidis E, et al. On the flow and vortex shedding characteristics of an in-line tube bundle in steady and pulsating crossflow, Chemical Engineering Research and Design, 78 (2000), pp. 1129-1138.

[15] Qi L. M, Experimental study on wake characteristics and vortex evolution of side-by-side circular cylinders placed near wall, M. D. thesis, Shanghai Instttute of Technology, Shanghai, China, 2023.

[16] Hsu L C, et al., Flow and Heat Transfer Characteristics of Staggered Cylinders[J]. Journal of Mechanics, 39 (2023), pp. 213-228.

[17] Yin P, et al., Numerical study on hydrodynamic interaction characteristics of vortex-induced vibration of two side-by-side cylinders near the wall, Ocean Engineering, 308 (2024), pp. 118305.

[18] Tao W. Q, Numerical heat transfer, Xi 'an Jiaotong University Press, Xian, China, 2002.

[19] Wilcox D C, Turbulence modeling for CFD, DCW industries, La Canada, 1998.

[20] Cheng K. M, et al., On Cause and Research Strategy of Flow Asymmetry in High-Alpha Flows, Nanjing University of Aeronautics and Astronautics, 34 (2002), pp. 17-21.

Submitted: 12.10.2024.

Revised: 15.01.2025.

Accepted: 01.03.2025.